Rev.Adv.Mater.Sci. 6 (2004) 131-139

# MECHANICAL PROPERTIES OF HIGHLY ORDERED NANOPOROUS ANODIC ALUMINA MEMBRANES

**Z. Xia[1], L. Riester[2], B. W. Sheldon[1], W. A. Curtin[1], J. Liang[1], A. Yin[1] and J. M. Xu[1]**

[1]Division of Engineering, Brown University, Providence, Rhode Island, 02912, USA
[2]Oak Ridge National Laboratory, Oak Ridge, Tennessee, 37831-6069, USA

*Received: February 25, 2004*

**Abstract.** Young's modulus, hardness and fracture toughness of highly ordered nanoporous alumina (PAA) were measured by nanoindentation and Vickers microindentation. A finite element model that accounts for the anisotropy and the pores was developed to extract the Young's modulus and hardness values from the experiments. The measured Young's modulus of 140 GPa was not affected by a heat treatment at 650 °C. However, the same heat treatment causes the hardness to increase from 5.2 to 6.3 GPa, while the fracture toughness sharply decreases from 3.4 to 0.4 MPa-$m^{1/2}$. When the indentation is made on the top surface of the membrane, nanopore collapse in shear bands rather than crack formation was observed around the indent. This suggests that the pores greatly improve the toughness of the porous alumina in the transverse direction. X-ray diffraction shows no sign of crystallization of the amorphous alumina after annealing at 650 °C. However, FTIR spectra show that the heat treatment significantly reduces the OH content of the amorphous structure. Thus it appears that the sharp reduction in the fracture toughness after annealing can be attributed to changes in the amorphous structure due to the loss of water.

## 1. INTRODUCTION

The formation of nanopores during the anodic oxidation of ultra-pure aluminium has been studied for more than 40 years [1]. Since Masuda [2] first reported the occurrence of a periodic pore arrangement in porous anodic alumina (PAA) in 1995, these materials have attracted considerable interest. Because of their unique pore structures, PAA has been widely used as a template for preparing nanostructures with a wide range of materials [3]. For example, porous alumina membranes have been used to fabricate highly ordered nanopore arrays as two-dimensional photonic crystals [4] or micropolarizers [5]. Moreover, PAA has been used as a template for the fabrication of polymeric nanostructures [6], nanometals [7-8], polymeric and carbon nanotubes [9-11]. Recently, we have observed unique deformation and fracture mechanisms in nanocomposite PAA films reinforced with highly ordered carbon nanotubes [12].

A detailed understanding of the mechanical properties of PAA films is an important part of our investigations of composite materials based on PAA. To date few studies have been conducted on the mechanical properties of PAA films. Alcala *et al.* [13] measured Young's modulus and hardness of barrier-type amorphous anodic oxides by nanoindentation. In the current paper we report mechanical properties including Young's modulus, hardness and fracture toughness ($K_{Ic}$) of highly ordered nanoporous alumina that were obtained by micro- and nano-indentation. The fracture mechanisms of the materials and effects of heat treatment on the mechanical properties of the materials were also investigated. Numerical models were developed to calculate Young's modulus and hardness of the

Corresponding author: B.W. Sheldon, e-mail: Brian_Sheldon@brown.edu

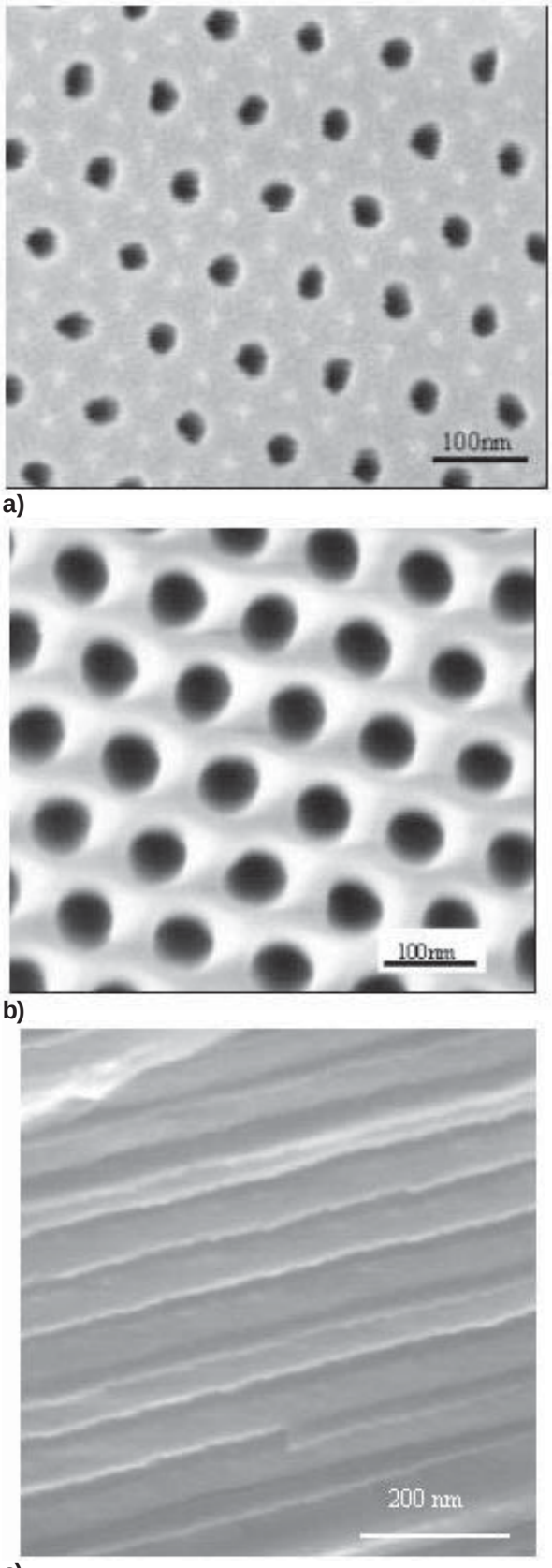


**Fig. 1.** SEM images of (a) as-fabricated 20 μm-thick alumina before widening process and (b) 90 μm-thick alumina after widening process, viewed from the top, showing a high degree of hexagonal order and (c) cross-section of 20 μm-thick alumina.

dense amorphous alumina. These results show that the heat treatment does not change the Young's modulus but strongly affect the fracture toughness of the alumina.

## 2. MATERIAL FABRICATION AND TESTING METHODS

Fabrication of the composites studied here follows the method in Ref. [11]. Briefly, high purity (99.99%) aluminum sheets are anodized in a multistep process to generate an amorphous nanoporous alumina matrix having a hexagonal array of straight pores extending from the substrate to the matrix surface. The samples studied here are 20 μm- or 90 μm-thick coatings. After anodization, the alumina pore diameters are in the range of 30-40 nm as shown in Fig. 1a. The nanopores are straight all the way from the top to bottom of the samples (Fig. 1c). During subsequent etching, there is further widening of the pore diameters to 50-60 nm. A scanning electron microscope (SEM) image of the top surface of the 90 μm-thick specimen is shown in Fig. 1b. In addition to characterizing specimens after anodization, we also studied identical samples that were subsequently heat treated at 645 °C in flowing Ar for 12 hours.

X-ray diffraction of the as-fabricated PAA does not show any evidence of crystallinity. There is no noticeable change in the diffraction pattern after the heat treatment, thus indicating that this material is also amorphous. Based on SEM images, the pore structure is also unchanged by the heat treatment. Fourier transform infrared (FTIR) spectroscopy was performed to look for evidence of water in the amorphous network. Transmission spectra for as-fabricated and heat-treated specimens are shown in Fig. 2. The broad band between 2700 and 3700 $cm^{-1}$ in the as-fabricated material indicates that substantial amounts of OH are present. This band is almost completely eliminated after the sample is heated to 645 °C, which indicates that this annealing has removed most of the OH from the material.

The specimens were subjected to nanoindentation, using a Nanoindenter® Model II with a Berkovitch indenter and a cube-cornered indenter, on the top and side of the porous alumina. The Berkovitch indenter was used primarily to measure hardness and elastic modulus. The sharper cube-corner indenter was employed so that cracks were most likely to be generated, and at the lowest possible loads. A standard Vickers microindenter on a Wilson microhardness tester (model Tukon 2100) was also used to measure the fracture toughness.

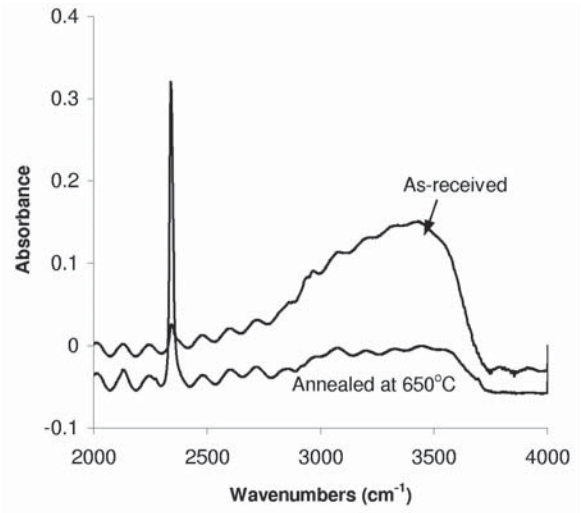


**Fig. 2.** Fourier transform infrared (FTIR) spectroscopy of as-fabricated and heat- treated anodic alumina thin films.

Loads of 20-650 mN were used for cube- cornered indentation and 500 g for Vickers micro-indentation. Indentation on the top surface generates planar cracks parallel to the pore axis. Cross-sections were obtained by embedding the samples in epoxy and polishing, thus allowing indentation on the side surfaces of the film, away from both the alumina/aluminum and alumina/epoxy interfaces. This side indentation generated planar cracks oriented roughly perpendicular to the pore axis. Thus, both dominant cracking modes were explored with these two test orientations. Indentation crack patterns and deformation were observed with a Hitachi S-4700 SEM.

Young's modulus for the porous film, $E_{eff}$, was calculated from the measured unloading tangent stiffness $S$ as

$$\frac{1-\nu^2}{E_{eff}} = \frac{2\beta\sqrt{A}}{\sqrt{\pi}S} - \frac{1-\nu_i^2}{E_i}, \qquad (1)$$

where $\beta$ is a constant which depends on the geometry of the indenter ($\beta$ =1.034 for Berkovich), ($E_{eff}$, $\nu$) and ($E_i$= 1100 GPa, $\nu_i$= 0.07) are the Young's modulus and Poisson's ratio for the specimen and Diamond indenter, respectively [14]. Implicit in the use of Eqs. (1) is the assumption of material isotropy. The hardness is obtained with

$$H = \frac{P}{A}, \qquad (2)$$

where $P$ is the applied load.

The fracture toughness of brittle materials can be conveniently measured by indentation. The fracture toughness $K_{Ic}$ can be calculated from the equation:

$$K_{Ic} = \alpha\left(\frac{E}{H}\right)^{1/2}\left(\frac{P}{c^{3/2}}\right), \qquad (3)$$

where $E$ and $H$ are the Young's modulus and hardness, respectively, $c$ is the radial crack length, and $\alpha$ is an empirical constant which depends on the geometry of the indenter. For cube-corner indenter, $\alpha$ = 0.04 and Vickers indenter $\alpha$ = 0.016 [15].

## 3. FINITE ELEMENT ANALYSIS

As noted above, Eq. (1) assumes material isotropy and is not immediately applicable since the porous material has a unidirectional structure that is elastically anisotropic. Proper extraction of the anisotropic moduli and the moduli of the constituent alumina requires careful attention to the details of the material system and a revision of Eq. (1) [16]. To accurately account for the anisotropy and the complexity of the indentation loading, we use a self-consistent multi-scale model that we developed for nanotube reinforced composites with an analogous structure [12]. An overview of the basic procedure is shown in Fig. 3.

We assume the solid is isotropic, and thus characterized by a Young's modulus $E$ and Poisson's ratio $\nu$. We then construct a fully-3d finite element model of an isotropic material containing aligned longitudinal pores in a hexagonal array. This model is subjected to both axial and transverse loadings to extract the elastic constants of the porous material in terms of the matrix material values. A second fully-3d FEM model is then used to represent the indentation geometry. A coating of the appropriate anisotropic homogenized porous material is placed on a thick pure aluminum substrate ($E$ = 70 GPa and $\nu$ = 0.3). An indentation mark is carved out, and symmetry permits the use of a reduced geometry, as shown in Fig. 3. Note that the plastic deformation associated with the indentation is ignored, since elasticity upon initial unloading should be independent of the prior plastic or permanent deformation. Very fine meshes are used around the indent area to limit inaccuracy. The indent holes are constructed to correspond to the experimental projected area $A$ and vertical indent distance $h$ and a diamond indenter having the same size as the indent hole is also constructed. The indenter and the material are connected with gap elements that allow the indenter to

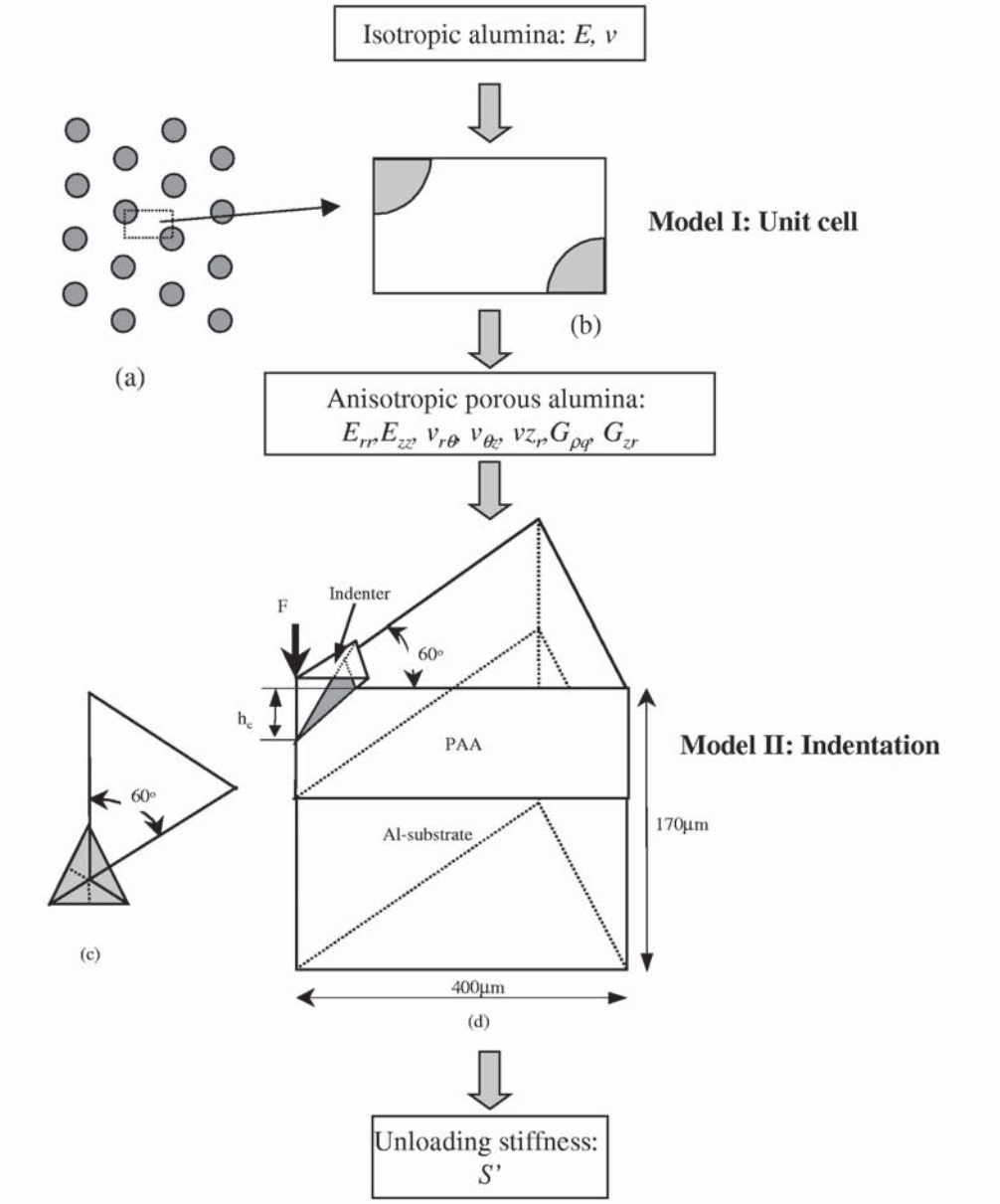


**Fig. 3.** Schematic of the multiscale finite element-based model for obtaining the constituent alumina elastic moduli from indentation measurements of the unloading stiffness *S'*.

slide along the interface. The coefficient of friction is chosen as 0.2 arbitrarily since it has little effect on the results. A small load *P* is applied on the top of the indenter and the displacement *u* of the indenter is then calculated using the finite element model. The unloading stiffness *S*'=*P*/*u* is then calculated and compared to the measured stiffness *S*, for both top and side indentation. Based on the differences between *S* and *S*', the elastic properties of the alumina matrix are modified and the procedure is iterated to self-consistency. The numerical models were verified by using isotropic material properties and comparing the FEM modulus values to those of Eq. (1).

## 4. RESULTS

### 4.1. Young's modulus and hardness

The 90 μm thick porous alumina coating was nanoindented along the coating cross section. The Young's moduli and hardness calculated with Eq. (1) and (2) versus the distance from the $Al/Al_2O_3$ interface are plotted in Figs. 4a and 4b. Both effective Young's moduli and hardness decrease with the

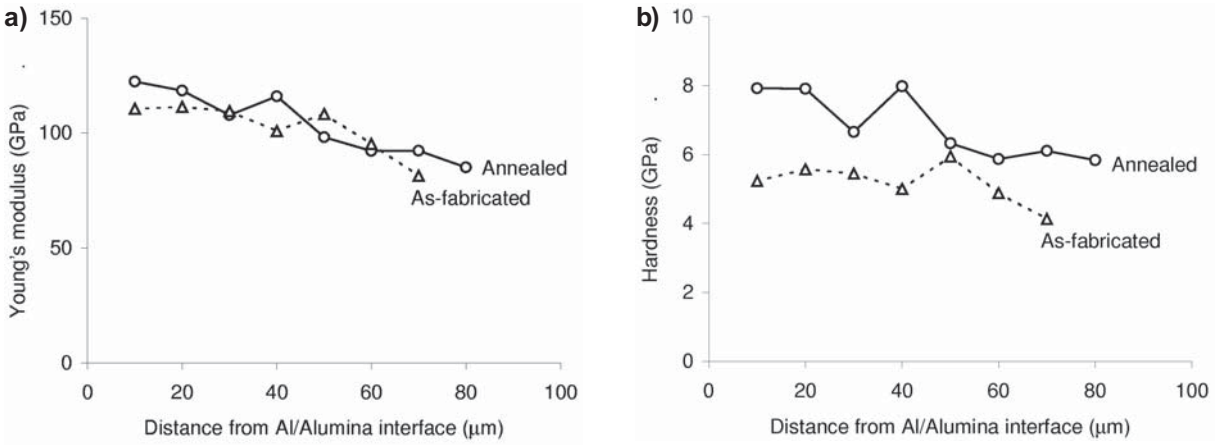


**Fig. 4.** Properties as a function of the distance from the Al/alumina interface for the 90 μm-thick specimen. (a) effective Young's modulus calculated with Eq. (1), (b) hard-ness of porous alumina calculated with Eq. (2).

distance away from the interface. The diameter of the pores at different positions, determined by SEM, is plotted in Fig. 5. Note that the pore size increases with the distance away from the interface. This widening appears to be associated with the anodization process that was used to produce the PAA. Based on the results in Figs. 4 and 5, the pore size change may at least partially cause the observed decrease of the Young's moduli and hardness. To determine how strong the pore size affects the alumina properties, we used the finite element model to calculate $E$ of the alumina, accounting for the pores. The results are plotted versus the distance in Fig. 5. It can be seen that the average value of $E$ for the alumina is approximately 140 GPa, with a small variation of less than 10% of the value. Since, $E$ is almost constant over the whole coating cross-section, it appears that the pore size is the primary factor leading to the observed variation of $E_{eff}$ and $H$.

The Young's moduli of the porous alumina on the top surface and side of the sample, calculated with Eq. (1) and the finite element model, are listed in Table 1. The effective Young's moduli and hardness measured here are close to the results reported by Alcala *et al.* [13]. The finite element results are close to the indentation modulus calculated with the standard method (Eq. (1)). The difference is due to the anisotropy that is not accounted for in the standard method. The moduli and hardness of solid alumina (no pores) as calculated using the finite element method are shown in Table 2. The alumina modulus of 140 GPa is consistent with the modulus of low-density irradiated alumina [17] and is lower than the typical values of 350-390 GPa for dense polycrystalline a alumina. As can be seen from Table 2, the heat treatment does not affect Young's modulus but it does increase the hardness of the porous alumina. After heat treatment, the hardness increases by 20%. The hardness is also over three times lower than that observed in a alumina.

## 4.2. Fracture Mechanisms and Fracture toughness

Micro- and nano-indentations were made on the top of the porous samples, but cracking was not observed at loads up to 9.8 N for microindentation and 650 mN for nanoindentation. A key feature is that in addition to the indentation mark, the deformation is

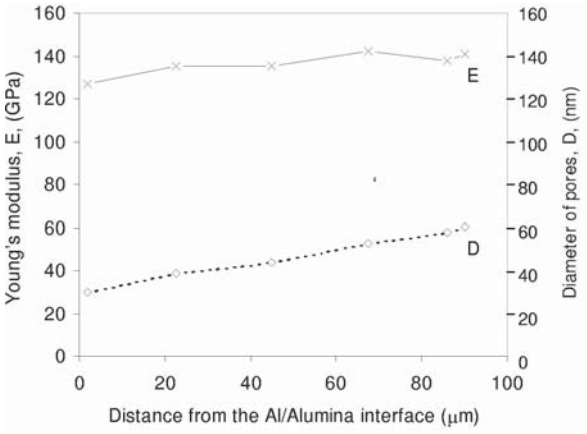


**Fig. 5.** Diameter of pores in 90 μm thick alumina and Young's modulus of the alumina calculated by the FEA as a function of distance from the Al/alumina interface.

**Table 1.** Mechanical properties of porous $Al_2O_3$ calculated by standard formula (Effective Modulus) and finite element model (FEM).

| Material | Treatment | Orientation | Average Pore Diameter (nm) | Hardness H (GPa) | Effective E (GPa) | FEM $E_{rr}$ or $E_{zz}$ (GPa) | $K_{Ic}$ (MPa-$m^{1/2}$) |
|---|---|---|---|---|---|---|---|
| 20μm-$Al_2O_3$ | As-fabricated | Side* | 37 | 5.0 | 104 | 93 | - |
| | | Top | 37 | 5.3 | 126 | 128 | - |
| 90μm-$Al_2O_3$ | As-fabricated | Side* | 50** | 5.2 | 107 | 74 | 2.4 |
| | | Top | 60.3 | 3.4 | 85 | 92 | - |
| 90μm-$Al_2O_3$ | Heat treatment | Side* | 50** | 6.8 | 104 | 75 | 0.28 |
| | | Top | 60.5 | 4.1 | 86 | 93 | - |

* in the middle of the sample

accommodated by shear collapse of rows of pores. Figs. 6a,b,c show the deformation at various scales. At large scales, as shown in Fig. 6a, a dark circular ring is observed around the indentation mark. Upon closer observation, this dark ring is caused by the scattering from short bands of collapsed pores, as seen in Fig. 6b. Further inspection shows the occurrence of shear cracks between opposite sides of neighboring collapsed pores, as seen in Fig. 6c. The pore collapse deformation mode is similar to shear band formation and to deformation modes observed in large-scale porous metals and polymers [18].

Micro-indentation and nano-indentation were also made on the side of 90 μm thick porous material. The as-fabricated alumina shows no crack until the load increases to a maximum of 650 mN. The crack patterns are shown in Fig. 7a. Cracks are also generated on the heat-treated sample at a load of as low as 100mN (Fig. 7b) but these cracks have rather complex patterns such as chips and deflection that are not valid for determining the fracture toughness by Eq. (3). Nevertheless, the results suggest that the porous alumina becomes far more brittle after annealing. For micro-indentation, regular cracks are generated in the heat-treated sample at a load of 500 g, as shown in Fig. 7c. However, it is important to note that this load does not produce cracks in the as-fabricated sample. At loads above 500 g, both the as-fabricated and heat-treated samples were crushed in the indentation due to the limited coating cross section.

**Table 2.** Mechanical properties of amorphous $Al_2O_3$ calculated by FEM (accounting for porosity).

| Treatment | *E* (GPa) | *H* (GPa) | $K_{Ic}$ (MPa-$m^{1/2}$) |
|---|---|---|---|
| As-fabricated | 141 | 5.2 | 3.4 |
| Heat treatment | 142 | 6.3 | 0.4 |

The fracture toughness of the porous alumina calculated using Eq. (3) is listed in Table 1. Accounting for the presence of the pores, the $K_{Ic}$ for the as-fabricated amorphous alumina material is 3.4 MPa-$m^{1/2}$. Although comparable to polycrystalline α alumina (~3 MPa-$m^{1/2}$), this is a high value for a non-crystalline ceramic. After the heat treatment, the mean value of $K_{Ic}$ drops to 0.4 MPa-$m^{1/2}$, much lower than that of the as-fabricated material, but comparable to other amorphous ceramics with a typical value of $K_{Ic}$ = 0.4-0.6 MPa-$m^{1/2}$ [15]. Note that our methodology for obtaining $K_{Ic}$ accounts for the void space due to the pores, but it does not treat pore collapse. Thus while the observed drop in $K_{Ic}$ reflects a real effect (i.e., longer indentation cracks in the heat-treated material), it is not clear whether the actual value is fully equivalent to $K_{Ic}$ for a dense, elastic solid. An assessment of this will require further investigation and verifaction.

## 5. DISCUSSION

Fig. 6 shows that the deformation around the indentation mark is accommodated by shear collapse of rows of pores. This type of behaviour is observed in both the as-fabricated and heat-treated specimens. The deformed shapes of the sheared pores indicate

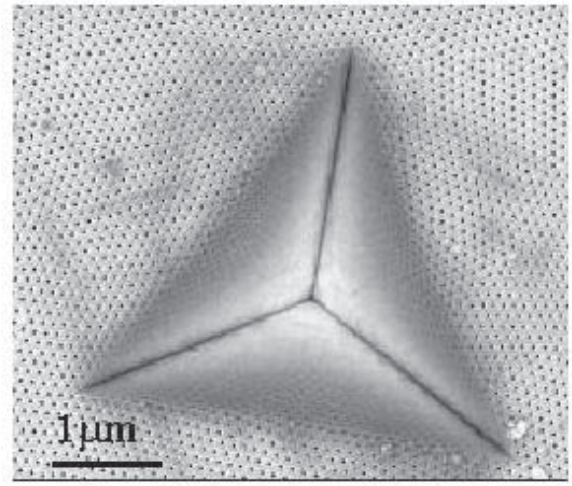


a)

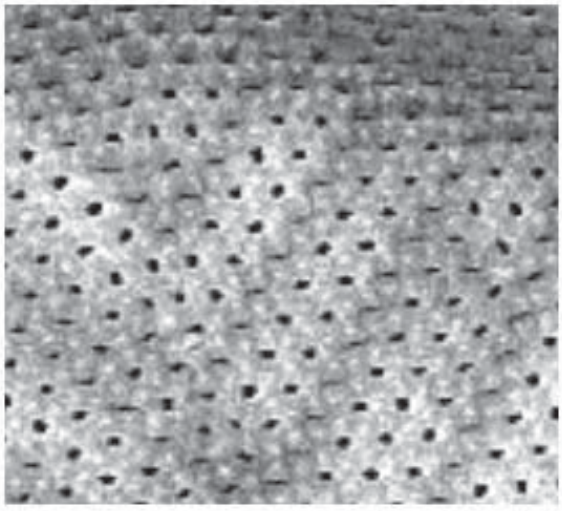

b)

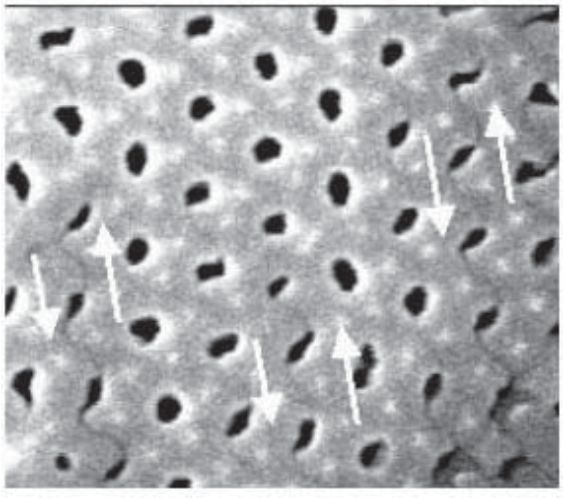

c)

**Fig. 6.** SEM images showing deformation in the porous alumina sample: (a) nanoindentation mark surrounded by dark circular regions; (b) array of 'shear bands' of collapsed pores causing dark regions; (c) close-up showing small shear cracks between collapsed pores in a shear band.

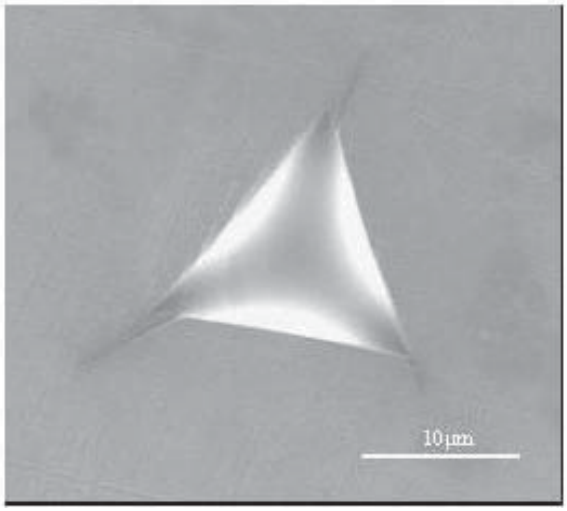


a)

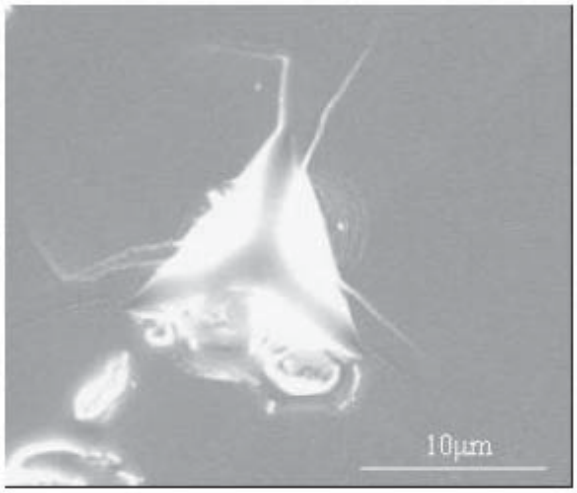


b)

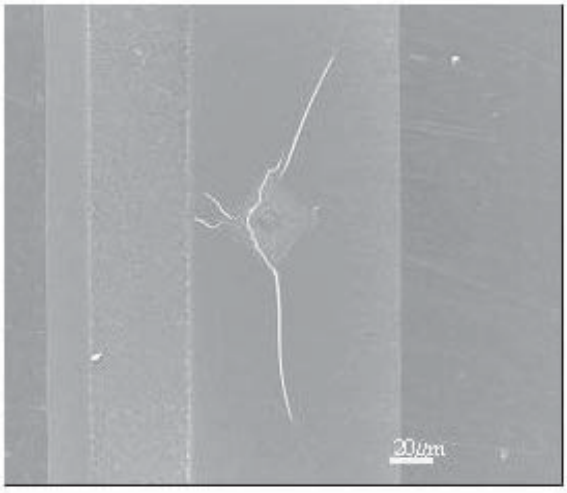


c)

**Fig. 7.** SEM images of indentation cracks generated on (a) as-fabricated porous alumina sample by side nanoindentation at a maximum load of 650 mN, (b) on heat-treated porous alumina sample by side nanoindentation at a load of 400 mN and (c) on side of heat-treated porous alumina sample by side Vickers micro-indentation at a load of 500 g.

that the shear cracks have formed only after substantial pore deformation. To accommodate the shear deformation there must be some flow of the alumina matrix. This is apparently possible in the amorphous alumina, although such flow is not normally expected in oxide materials at macroscopic scales, room temperature, and under the expected loads around the indent mark. However, similar unexpectedly high flow rates have been deduced in studies of relaxation of thin films with nanoscale subsurface silica layers [24]. Since silica has gross mechanical properties similar to those deduced for the present alumina matrix, it is possible that related mechanisms are operating in both of these amorphous oxides.

The results in Fig. 4 and Table 2 show that the heat treatment strongly affects $H$ and $K_{Ic}$ but not $E$. After annealing, the Young's modulus of the alumina shows no sign of change, the hardness increase by 20% while the fracture toughness decreases sharply from 3.4 to 0.4 MPa-m$^{1/2}$. Based on the FTIR results in Fig. 2, the observed properties variations may be caused by the water in the alumina. These FTIR results are consistent with other measurements in the literature. For example, Lamparter *et al*. investigated anodic alumina that initially contained 15% $H_2O$, and reported that at roughly 300 °C the water absorbed in the pores was released, and above 500 °C the water in the bulk has been removed [19]. Experiment, reverse Monte Carlo calculation and molecular dynamics simulations show that amorphous anodic alumina structure is dominated by slightly-distorted $(AlO_4)^{5-}$ tetrahedron [19-23]. Introduction of $H_2O$ is likely to interrupt the $AlO_4$ network structure. Analogous effects have been widely studied in silicate glasses, where this type of disruption of the network structure can be correlated with decreases in viscosity. Similar effects may occur in amorphous alumina, although the bonding is more ionic in this case. The lower hardness in the as-fabricated material is potentially consistent with an increase in viscous deformation at the high stresses under the indenter. The relatively high $K_{Ic}$ is more difficult to interpret. To our knowledge, hydration effects are not known to produce such fracture toughness values in silicate glasses. One possible interpretation for our results is that the porosity contributes to additional toughening in the as-fabricated sample, but that this effect is absent after the heat-treatment. This difference could involve viscous deformation, since the pore collapse and shear banding observed under different loading (Fig. 6) indicates that some flow can occur in these materials. However, the difference in the $K_{Ic}$ values obtained from the side indents would then have to be reconciled with the observation that the top indents produce similar shearing of the pores in both materials. Further investigation of these effects is clearly warranted, with more detailed consideration of the possible role of hydration and structural defects in the alumina

In summary, our results show that porous anodic alumina exhibits toughening behaviour that is not generally observed in dense amorphous oxides. While the high mobility of structural defects leads to high ductility and inhibits the propagation of cracks in metals, the absence of these mechanisms in ceramics generally leads to low toughness and catastrophic failure by brittle fracture. However, the pore collapse and shear banding observed in Fig. 6 allows the material to reduce high stress concentration and absorb significant amounts of energy. As a result, the nanoporous materials become tougher in the transverse direction. In particular, this behaviour occurs in the heat treated material, where our measurements and modelling show that the inherent fracture toughness of the dense alumina is very low. The high $K_{Ic}$ value for the as-fabricated material is another indication of toughening. It should be emphasized that this increase is distinct from the pore collapse and shear banding in Fig. 6, which is observed in materials with both high and low $K_{Ic}$.

## 6. CONCLUSIONS

Young's modulus, hardness and fracture toughness of highly ordered nanoporous alumina (PAA) were measured by nanoindentation and Vickers microindentation. A finite element model accurately accounting for the anisotropy and pores was used to extract the Young's modulus and hardness of amorphous alumina (no-pore). The principal results are

1) Accounting for pores, Young's modulus of the alumina is determined as 140 GPa. Heat treatment at 650 °C does not affect the Young's modulus.
2) After annealing hardness of the alumina increases from 5.2 to 6.3 GPa while the fracture toughness decreases from 3.4 to 0.4 MPa-m$^{1/2}$.
3) In top indentation on the porous alumina, nanopore collapse in 'shear bands', rather than crack formation was observed around the indent, suggesting that the pores in the alumina lead to a higher toughness in the transverse direction.

## ACKNOWLEDGEMENTS

The authors at Brown University acknowledge support of this work through a grant from the Ultra Efficient Engine Technology (UEET) program at NASA Glenn Research Laboratory. This work was also supported by the National Science Foundation under Award Number CMS-0304246. The material fabrication group at Brown was supported by DARPA NMASP program. Research also sponsored by the Assistant Secretary for Energy Efficiency and Renewable Energy, Office of FreedomCAR and Vehicle Technologies, as part of the High Temperature Materials Laboratory User Program, Oak Ridge National Laboratory, managed by UT Battelle, LLC, for the U.S. Department of Energy under contract number DE-AC05 00OR22725. G.C. Wang and G.T. Palmore are acknowledged for conducting the FTIR measurements.

## REFERENCES.

[1] J.W.Diggle, T.C.Downie and C.W.Goulding // *Chem Rev.* **69** (1969) 369.
[2] H. Masuda and K. Fukuda // *Science* **268** (1995)1466.
[3] A.Huczko // *Appl. Phys.* **A70** (2000) 365.
[4] A. P.Li, F.Muller, A.Birner, K.Nielsch and U.Gosele // *Adv. Mater*. **11** (1999) 483.
[5] M.Saito, M.Kirihara, T.Taniguchi and M.Miyagi // *Appl. Phys. Lett*. **55** (1989) 607.
[6] S. De Vito and C.R. Martin // *Chem. Mater*. **10** (1998) 1738.
[7] B.Z. Tang and H.Xu // *Macromoleculaes*, **32** (1999) 2569.
[8] J.C.Hulteen and C.R.Martin // *J. Mater. Chem*. **7** (1997) 1075.
[9] M. Steinhart *et al.*// *Science* **296** (2002) 1997.
[10] C. R. Martin // *Chem. Mater.* **8** (1996) 1739; H. Masuda and M. Satoh // *Jpn. J. Appl. Phys.*, Part 2 35 (1996) L126; D. Routkevitch, A. A. Tager, J. Harujama, D. Almawlawi, M. Moskovits and J. M. Xu // *IEEE Trans. Electron Devices* **40** (1996) 1646.
[11] J. Li, C. Papadopoulos, J.M. Xu and M. Moskovits // *App. Phy. Lett.* **75** (1999) 367.
[12] Z. Xia, L. Riester, W.A. Curtin, H. Li, B.W. Sheldon, J. Liang, B. Chang and J.M. Xu // *Acta Mater*. To appear in 2004.
[13] G. Alcala, P. Skeldon, G.E. Thompson, A.B. Mann, H. Habazaki and K. Shimizu // *Nanotechnology* **13** (2002) 451.
[14] W.C. Oliver and G.M Pharr // *J. Mater. Res.* **7** (1992) 1564.
[15] G. M. Pharr // *Mater. Sci. Eng.* **A253** (1998) 151.
[16] J.J. Vlassak and W.D. Nix // *Phil.Mag.* **67** (1993) 1045.
[17] J.C. Barbour, J.A. Knapp, D.M. Follstaedt T.M. Mayer, K.G. Minor and D.L. Linam // *Nuclear Instrument & Methods in Physics Research* **166** (2000) 140.
[18] S.D. Papka and S. Kyriakides // *Acta Materialia* **46** (1998) 2765; N. Triantifyllidis and M. Schraad // *Journal Mech. Physics Solids* **46** (1998) 1089.
[19] P. Lamparter and R. Kniep // *Physica* **B234-236** (1997) 405.
[20] Y. Oka, T. Takahashi, K. Okada and S. Ichi Iwai // *J. Non-Cryst. Solids* **30** (1979) 349.
[21] S.M. El-Mashri, S.M. El-Mashri and A.J. Forty // *Philos. Mag.* **A49** (1984) 341.
[22] A.J. Bourdillon, R.G. Jones and A.J. Forty // *Philos. Mag.* **A48** (1983) 665.
[23] G. Gutierrez and B. Johansson // *Physical Rev.* **B 65** (2002) No.104202.
[24] R. Huang, H. Yin, J.Liang, J.C. Sturm, K.D. Hobart and Z. Suo // *Acta Mech. Sin.* **18** (2002) 441.